SPECTRAL METHODS FOR PARTIAL DIFFERENTIAL EQUATIONS IN IRREGULAR DOMAINS: THE SPECTRAL SMOOTHED BOUNDARY METHOD[*]

ALFONSO BUENO-OROVIO[†], VÍCTOR M. PÉREZ-GARCÍA[†], AND FLAVIO H. FENTON[‡]

Abstract. In this paper, we propose a numerical method to approximate the solution of partial differential equations in irregular domains with no-flux boundary conditions. The idea is to embed the domain into a box and use a smoothing term to encode the boundary conditions into a modified equation that can be approached by standard spectral methods. The main features of this method are its capability to deal with domains of arbitrary shape and its easy implementation via fast Fourier transform routines. We discuss several examples of practical interest and test the results against standard numerical methods.

Key words. spectral methods, irregular domains, phase field methods, reaction-diffusion equations

AMS subject classifications. 65M70, 65T50

DOI. 10.1137/040607575

1. Introduction. Spectral methods [1, 2, 3] are among the most extensively used methods for the discretization of spatial variables in partial differential equations and have been shown to provide very accurate approximations of sufficiently smooth solutions. Because of their high-order accuracy, spectral methods have become widespread over the years in various fields, including fluid dynamics, quantum mechanics, heat conduction, and weather prediction [4, 5, 6, 7, 8]. However, these methods have some limitations which have prevented them from being extended to many problems, where finite-difference and finite-element methods continue to be used predominantly. One limitation is that the discretization of partial differential equations by spectral methods leads to the solution of large systems of linear or nonlinear equations involving full matrices. Finite-difference and finite-element methods, on the other hand, lead to systems involving sparse matrices that can be handled by appropriate methods to reduce the complexity of the calculations substantially. Another drawback of spectral methods is their inability to handle irregularly shaped domains, which is why these methods have had limited use in many engineering problems, where finite-element methods are preferred because of their flexibility in describing complex geometries despite the computational costs associated with constructing an appropriate solution grid. Although there have been attempts to use spectral methods in irregular domains [9, 10], these approaches usually involve either incorporating finite-element preconditioning or using the so-called spectral elements. We are not aware of any

[†]Departamento de Matemáticas, Universidad de Castilla–La Mancha, E.T.S.I. Industriales, Av. Camilo José Cela, 3, Ciudad Real, E-13071, Spain (alfonso.bueno@uclm.es, victor.perezgarcia@uclm.es). The work of the first author was supported by CCyT–JCCM under Ph.D. grant 03-056. The work of the first author was also partially supported by NSF grant 0320865.

[‡]Department of Biomedical Sciences, Cornell University, Ithaca, NY 14853, and Beth Israel Medical Center, New York, NY (fhf3@cornell.edu).

previous study in which purely spectral methods, particularly those involving fast Fourier transforms (FFTs), have been used to obtain solutions in complex irregular geometries.

In this paper we present an easy-to-use method for approximating the solution of partial differential equations in irregular domains with no-flux boundary conditions using spectral methods. The idea is based on what, in dendritic solidification, is known as the phase-field method [11]. This method is used to locate and track the interface between the solid and liquid states and has been applied to a wide variety of problems including viscous fingering [12, 13], crack propagation [14], and the tumbling of vesicles [15]. For a comprehensive review see [16].

In what follows we use the idea behind phase-field methods to illustrate how the solution of several partial differential equations can be obtained in irregular domains using spectral methods, understanding for irregular any arbitrarily shaped domain beyond the standard rectangular or circular geometries. Throughout, for simplicity, we will refer to the combination of the phase-field and spectral methods as the spectral smoothed boundary (SSB) method. Our approach consists of two steps. First, the idea of the phase-field method is formalized and its convergence analyzed for the case of homogeneous Neumann boundary conditions. Then we discuss how the new formulation is useful for the direct use of spectral methods, specifically those based on trigonometric polynomials. This formulation makes the problem suitable for efficient solution using FFTs [17]. Since it is our intention that the resulting methodology be used in a variety of problems in engineering and applied science, we have concentrated on the important underlying concepts, reserving some of the more formal questions related to these methods for a subsequent analysis.

2. The phase-field (smoothed boundary) method. In this work we focus on applying the phase-field method to partial differential equations of the form

$$(2.1a) \qquad \nabla(\boldsymbol{D}^{(j)}\nabla u_j) + f(u_1, \ldots, u_N, t) = \partial_t u_j$$

for N unknown real functions u_j defined on an irregular domain $\Omega \subset \mathbb{R}^n$, where $n = 1, 2, 3$ is the spatial dimensionality of the problem, together with appropriate initial conditions $u_j(x, 0) = u_{j0}(x)$ and subject to Neumann boundary conditions

$$(2.1b) \qquad \vec{\boldsymbol{n}} \cdot \boldsymbol{D}^{(j)}\nabla u_j = 0$$

on $\partial\Omega$, where $\boldsymbol{D}^{(j)}(x)$ is a family of $n \times n$ matrices that may depend on the spatial variables. Equations (2.1a) and (2.1b) include many reaction-diffusion models, such as those describing population dynamics or cardiac electrical activity. Here we will restrict the analysis to equations of the form (2.1a), although the idea behind the method can be extended to many other problems involving complex boundaries and different types of partial differential equations.

Instead of discretizing (2.1a), the smoothed boundary method (SBM) relies on considering the auxiliary problem

$$(2.2) \qquad \nabla(\phi^{(\xi)}\boldsymbol{D}^{(j)}\nabla u_j^{(\xi)}) + \phi^{(\xi)}f(u_1^{(\xi)}, \ldots, u_N^{(\xi)}, t) = \partial_t(\phi^{(\xi)}u_j^{(\xi)})$$

for the unknown functions $u_j^{(\xi)}$ on an enlarged domain Ω' satisfying the following conditions: (i) $\Omega \subset \Omega'$ and (ii) $\partial\Omega \cap \partial\Omega' = \emptyset$. The function $\phi^{(\xi)}$ is continuous in Ω' and has the value one inside Ω and smoothly decays to zero outside Ω, with ξ

identifying the width of the decay. That is, if χ_Ω is the characteristic function of the set Ω defined as

$$(2.3) \qquad \chi_\Omega = \begin{cases} 1, & x \in \Omega, \\ 0, & x \in \Omega' \backslash \Omega, \end{cases}$$

then $\phi^{(\xi)} : \Omega' \to \mathbb{R}$ is a regularized approximation to χ_Ω such that $\lim_{\xi \to 0} \phi_\xi = \chi_\Omega$.

The key idea of the SBM is that when $\xi \to 0$, the solutions $u_j^{(\xi)}$ of (2.2) on any domain Ω' with arbitrary boundary conditions on $\partial\Omega'$ satisfy $u_j^{(\xi)} \to u_j$; in other words, they tend pointwise to the solution of (2.1a), automatically incorporating the boundary conditions (2.1b). To see why, let us first realize that inside Ω the statement is inmediate since $\phi^{(\xi)} \to 1$ in Ω as $\xi \to 0$ and (2.2) becomes (2.1a). At the boundary, we consider for simplicity the situation with $n = 2$ (the extension to $n = 3$ is immediate). Assuming smoothness of $\partial\Omega$ (which in this case will be a curve) and choosing any connected curve $\Gamma \subset \partial\Omega$, we define two families of differentiable curves $\Gamma_{\delta(+)} \subset \Omega' \backslash \Omega$ and $\Gamma_{\delta(-)} \subset \Omega$ whose ends coincide with those of Γ and which tend uniformly to Γ following the parameter δ. The curves $\Gamma_{\delta(+)}$ and $\Gamma_{\delta(-)}$ are then the boundaries of a region A_δ whose boundary $\partial A_\delta = \Gamma_{\delta(+)} \cup \Gamma_{\delta(-)}$ (see Figure 2.1).

We now integrate (2.2) over A_δ:

$$(2.4) \qquad \int\int_{A_\delta} \left[\nabla(\phi^{(\xi)} \boldsymbol{D}^{(j)} \nabla u_j^{(\xi)}) + \phi^{(\xi)} f(u, t) \right] dx = \int\int_{A_\delta} \partial_t(\phi^{(\xi)} u_j^{(\xi)}) dx.$$

Using the Gauss (or Green) theorem for the first term of (2.4), we obtain

$$(2.5) \qquad \oint_{\partial A_\delta} \boldsymbol{\vec{n}} \cdot \phi^{(\xi)} \boldsymbol{D}^{(j)} \nabla u_j^{(\xi)} dx + \int\int_{A_\delta} \phi^{(\xi)} f(u, t) dx = \int\int_{A_\delta} \partial_t(\phi^{(\xi)} u_j^{(\xi)}) dx,$$

where $\oint$ denotes a line integral over ∂A_δ.

Now we take the limit $\xi \to 0$ in (2.5) to obtain

$$
\begin{aligned}
\lim_{\xi \to 0} \oint_{\partial A_\delta} \boldsymbol{\vec{n}} \cdot \phi^{(\xi)} \boldsymbol{D}^{(j)} \nabla u_j^{(\xi)} dx &= -\lim_{\xi \to 0} \int\int_{A_\delta} \phi^{(\xi)} f(u, t) dx \\
&\quad + \lim_{\xi \to 0} \int\int_{A_\delta} \partial_t(\phi^{(\xi)} u_j^{(\xi)}) dx \\
(2.6) \qquad &= m(A_\delta) \left[-\phi^{(\xi)} f(u, t) + \partial_t(\phi^{(\xi)} u_j^{(\xi)}) \right]_{x=\zeta},
\end{aligned}
$$

where the last equality comes from the mean value theorem for integrals and $m(A_\delta)$ is the measure of the set A_δ. Here we assume that the solutions to (2.2) and its time derivatives are bounded so that the right-hand side of (2.6) is finite. On the left-hand side we decompose $\oint_{\partial A_\delta}$ as $\int_{\Gamma_{\delta(+)}} + \int_{\Gamma_{\delta(-)}}$. It is straightforward that $\lim_{\xi \to 0} \int_{\Gamma_{\delta(+)}} \boldsymbol{\vec{n}} \cdot \phi^{(\xi)} \boldsymbol{D}^{(j)} \nabla u_j^{(\xi)} dx = 0$, since in this limit $\phi^{(\xi)} = 0$ over all $\Gamma_{\delta(+)}$ and $\phi^{(\xi)} = 1$ on $\Gamma_{\delta(-)}$. As we were interested in proving that the boundary conditions are satisfied, we now make the width of the integration region A_δ tend to zero. Since $\Gamma_{\delta(-)} \to \Gamma$ as $\delta \to 0$, and $\lim_{\delta \to 0} m(A_\delta) = 0$, we obtain

$$
\begin{aligned}
\lim_{\delta \to 0} \lim_{\xi \to 0} \oint_{\partial A_\delta} \boldsymbol{\vec{n}} \cdot \phi^{(\xi)} \boldsymbol{D}^{(j)} \nabla u_j^{(\xi)} dx &= \lim_{\delta \to 0} \int_{\Gamma_{\delta(-)}} \boldsymbol{\vec{n}} \cdot \boldsymbol{D}^{(j)} \nabla u_j^{(\xi)} dx \\
(2.7) \qquad &= \int_\Gamma \boldsymbol{\vec{n}} \cdot \boldsymbol{D}^{(j)} \nabla u_j^{(\xi)} dx = 0.
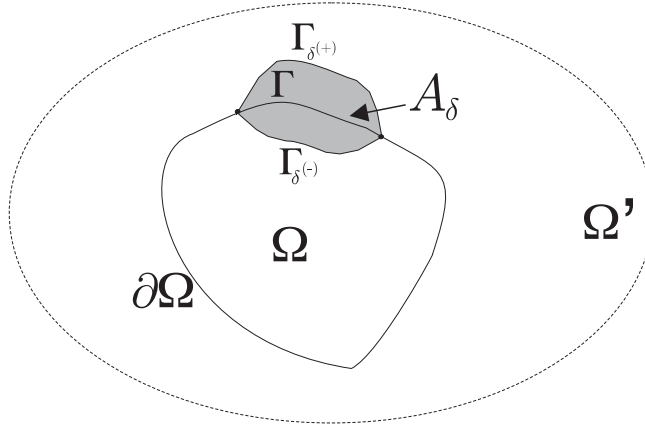\end{aligned}
$$

FIG. 2.1. *Illustration of an irregular domain Ω with an example of the connected curve Γ and the domain A_δ used in the proof of convergence of the method.*

Since (2.7) is true for any boundary segment Γ, we obtain the final result that, in the limit $\xi \to 0$, (2.2) satisfies $\vec{n} \cdot \boldsymbol{D}^{(j)} \nabla u_j^{(\xi)} = 0$ for $j = 1, \ldots, N$, i.e., the boundary conditions.

The idea of the SBM is then to consider (2.2) for a small but finite ξ and to discretize this problem instead of (2.1a) and (2.1b). The main advantage is that one can search for the approximation $u^{(\xi)}$ on any enlarged domain Ω' such that $\Omega \subset \Omega'$. The enlarged discrete problem can then be solved with any proper boundary conditions on $\partial \Omega'$, since the fulfillment of the boundary conditions for u on $\partial \Omega$ is guaranteed in the limit $\xi \to 0$.

3. The SSB method. We want to discretize (2.2) on an enlarged domain Ω', chosen to be a rectangular region containing Ω, and we will expand $u^{(\xi)}$ in the basis of Cartesian products of trigonometric polynomials $e^{ik_x x} e^{ik_y y}$. Thus, we will seek an extension of the solution u of (2.1a) and (2.1b) that is periodic on the enlarged region Ω'.

Note that since $\phi^{(\xi)}$ is located inside the time derivative of the right term of (2.2), it is possible for the integration domain itself to evolve in time, and thus this method could be used to solve moving boundary problems once a coupling equation is added for the movement of $\phi^{(\xi)}$. However, here we will deal only with stationary integration domains; thus, $\partial_t \phi^{(\xi)} = 0$ and the right side of (2.2) can be simplified as $\phi^{(\xi)} \partial_t u_j^{(\xi)}$. Dividing (2.2) by $\phi^{(\xi)}$, we get

$$(3.1) \qquad \nabla \log \phi^{(\xi)} \cdot \boldsymbol{D}^{(j)} \nabla u_j^{(\xi)} + \nabla(\boldsymbol{D}^{(j)} \nabla u_j^{(\xi)}) + f(u^{(\xi)}, t) = \partial_t u_j^{(\xi)},$$

which is an easier version of the equation of the SBM that we will use here to perform the numerical simulations.

To implement numerically any solution method for (3.1), we need to make a specific choice for $\phi^{(\xi)}$. In practice, any method that produces a smooth characteristic function can be used. In the context of phase-field methods, the standard procedure for obtaining the values of $\phi^{(\xi)}$ (which is called the "phase-field") is to integrate an auxiliary diffusion equation of the form $\partial_t \phi = \xi^2 \Delta \phi + (2\phi - 1)/2 - (2\phi - 1)^3/2$, with initial conditions $\phi^{(\xi)}(t = 0) = \chi_\Omega$, until a steady state is reached [16, 18]. Alternatively, since we seek only a smoothed boundary, we choose to obtain $\phi^{(\xi)}$ from

χ_Ω using a convolution of the form

$$(3.2) \qquad\qquad \phi^{(\xi)} = \chi_\Omega * G^{(\xi)},$$

where $G^{(\xi)}$ is any family of functions such that $\lim_{\xi\to 0} G^{(\xi)}(x) = \delta(x)$, with $\delta(x)$ being the Dirac delta function. In particular, Gaussian functions of the form

$$(3.3) \qquad\qquad G^{(\xi)}(x) = \prod_{k=1}^{n} \exp(-x_k^2/\xi^2)$$

can be chosen. In this paper, all the functions $\phi^{(\xi)}$ have been obtained using this n-dimensional discrete convolution given by (3.3), which also have the advantage of being efficiently computed using FFTs. An example of the creation of $\phi^{(\xi)}$ is shown in Figure 3.1, where it can be seen that the width of the interface in which $\phi^{(\xi)}$ changes from zero to one depends on the value used for ξ (in fact, it is of order ξ).

To avoid computational difficulties for very small values of $\phi^{(\xi)}$, we approximate $\log \phi^{(\xi)} \approx \log(\phi^{(\xi)} + \epsilon)$, where ϵ is the machine precision. Numerically, $\phi^{(\xi)}$ and $(\phi^{(\xi)} + \epsilon)$ are equal up to roundoff errors, but this correction bounds the value of $\log \phi^{(\xi)}$ as $\phi^{(\xi)} \to 0$. Due to the effect of the boundaries in the numerical stability of the scheme, we also need a reasonable margin between the boundaries of the physical and the enlarged domains. We found that a margin of value $M = 10\xi$ is sufficient for all the simulations to be stable [19]. Finally, all the spatial derivatives of $u^{(\xi)}$ in (3.1) are computed in Cartesian coordinates using differentiation in Fourier space, which as mentioned previously implicitly assumes periodic boundary conditions on $\partial \Omega'$. It is significant that only Fourier transforms are used for these calculations instead of differentiation matrices, thereby avoiding the generation and storage of these matrices and yielding more efficient codes and shorter execution times, especially when FFT routines are used.

In this paper, we are not concerned with designing the most efficient implementation of the SSB method, but only with proving that such a method can be used to integrate partial differential equations in irregular domains. Thus, for time integration we use a simple second-order explicit method. In the particular case when all the coefficients of the diffusion tensor $\boldsymbol{D^{(j)}}$ are constants, we can write (3.1) in the form

$$(3.4) \qquad\qquad \mathcal{L}u^{(\xi)} + \mathcal{N}(u^{(\xi)}, t) = \partial_t u^{(\xi)},$$

where $\mathcal{L}u^{(\xi)} = \nabla(\boldsymbol{D^{(j)}} \nabla u_j^{(\xi)})$ is the linear part of the equation, while the nonlinear term is represented by $\mathcal{N}(u^{(\xi)}, t) = \nabla \log \phi^{(\xi)} \cdot \boldsymbol{D^{(j)}} \nabla u_j^{(\xi)} + f(u^{(\xi)}, t)$. Then a second-order in time operator splitting scheme of the form

$$(3.5) \qquad\qquad U^{(\xi)}(t + \Delta t) = e^{\mathcal{L}\Delta t/2} e^{\mathcal{N}\Delta t} e^{\mathcal{L}\Delta t/2} U^{(\xi)}(t)$$

can be used to solve the equation in time [20]. For the examples to be presented later, we solve the nonlinear term by a second-order (half-step) explicit method and integrate the linear part exactly in Fourier space by exponential integration, which reduces the stiffness of the problem considerably and allows for the use of larger time steps.
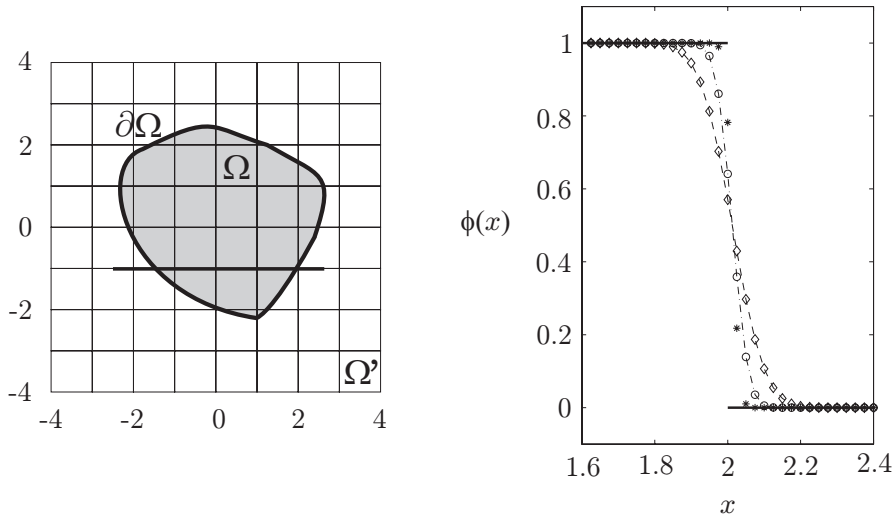
FIG. 3.1. *Left: Example of an irregular domain Ω defined on a Cartesian grid and an enlarged domain Ω'. Right: Smoothing of the irregular boundary in a one-dimensional section of the domain. The solid line on the right shows a small section of the characteristic function χ_Ω (with value 0 or 1) corresponding to part of the thicker line shown in the left part of the figure. Smoothed boundary functions $\phi^{(\xi)}$ obtained from χ_Ω for $\xi = 0.10$, 0.05, and 0.025 are labeled by diamonds, circles, and stars, respectively.*

4. Examples of the methodology.

4.1. The heat equation. As a first example, we will consider a simple linear heat equation. This first case will allow us to make a quantitative study of the errors of the SSB method. Specifically, we are interested in solving the following heat equation with sources:

$$(4.1) \qquad \partial_t u = D\Delta u - r\cos(2\theta)$$

in the annulus Ω defined by $1 \leq r \leq 2$ with homogeneous Neumann boundary conditions on $\partial\Omega$, $\partial_r u|_{r=1} = \partial_r u|_{r=2} = 0$. The diffusion coefficient is taken to be constant with value $D = 1$. Figure 4.1 shows one example of the generation of the smoothed boundary for this domain.

Equation (4.1) in this geometry has an explicit steady state solution of the form

$$(4.2) \qquad u_{st}(r,\theta) = \left(\frac{1}{5}r^3 - \frac{31}{50}r^2 - \frac{8}{25}\frac{1}{r^2}\right)\cos(2\theta),$$

which can be used to determinate the contribution to the error introduced by the smoothing term in (2.2). Thus, (4.1) is evolved in time using the SSB method and this explicit steady state as initial data until the new steady state is reached and deviations from the initial condition are measured. Figure 4.2 (left) shows the L^2-norm of the error of several simulations for different values of ξ and grid resolutions. Note that in general these maximum errors decrease as the thickness of the interface is reduced. The left and right interior plots show the log-log plots of the L^2-norm of the error versus ξ (values at $\eta = 5$, see below), indicating an $O(\xi^2)$ accuracy of the method as $\xi \to 0$ when the integration domain Ω does not have sharp corners.
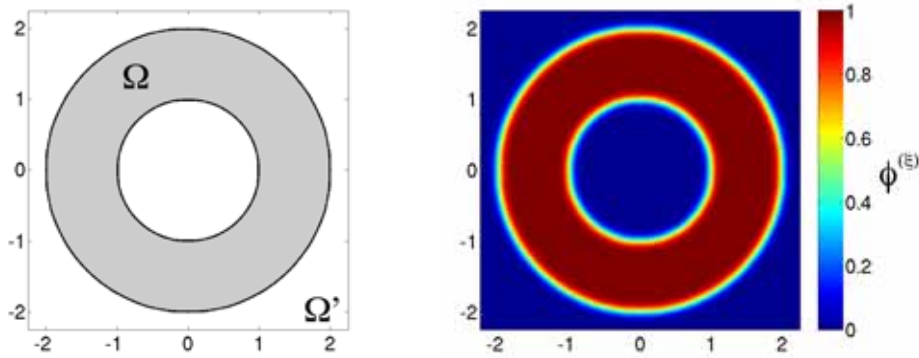
FIG. 4.1. *Left: The rectangular domain Ω' in which (4.1) is solved using the SSB method, with the irregular domain Ω (an annulus) shown in gray. Right: Smoothed boundary function $\phi^{(\xi)}$ given by (3.2) for $\xi = 0.10$.*
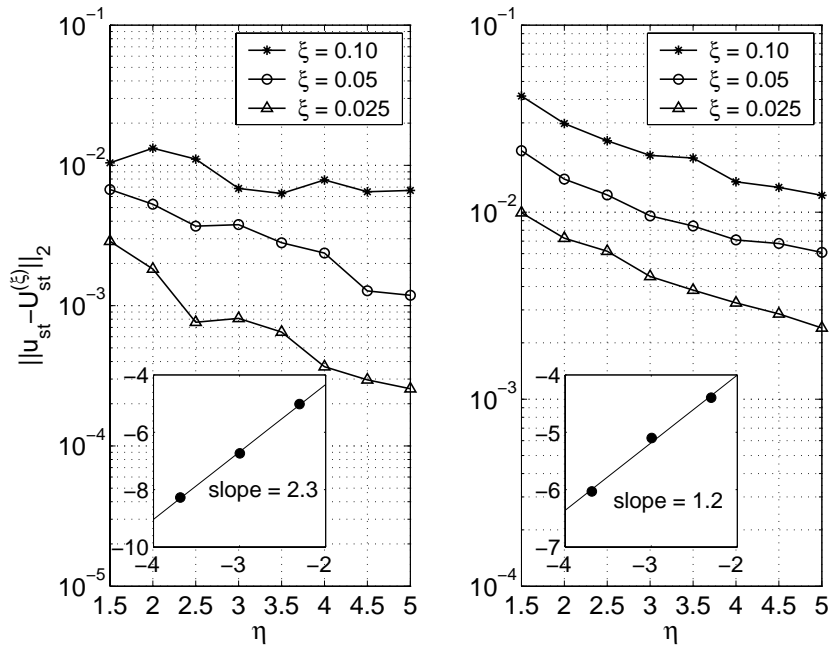

FIG. 4.2. *Left: L^2-error of the numerical steady state solution of (4.1) in the annulus compared to the exact steady solution as a function of the parameter $\eta = \xi/\Delta x$. Right: Same as left but for the quarter-annulus geometry. See text for details.*

Although $\phi^{(\xi)}$ is a continuous function, it is necessary to have a grid fine enough to properly resolve the boundary layers in which it quickly changes from zero to one. For this reason, errors are represented in Figure 4.2 not as a function of the number of grid points but as a function of the parameter $\eta = \xi/\Delta x$, which gives an idea of the number of points that lie in the interface (with number of points varying in this case from 90 to 300 points for $\xi = 0.10$, from 150 to 500 points for $\xi = 0.05$, and from 270 to 900 points for $\xi = 0.025$). To ensure that this error is produced only by the spatial
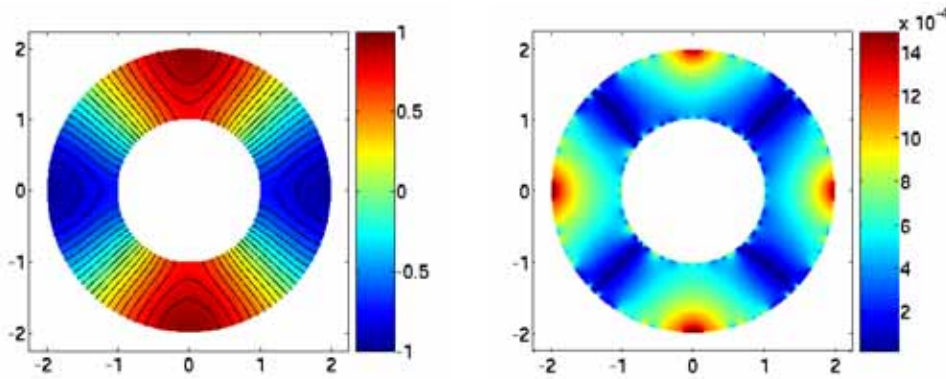
FIG. 4.3. *Left: Solution of* (4.1) *obtained with the SSB method at steady state in the annulus* $1 \le r \le 2$. *Grid size is* 540×540 *with* $\xi = 0.025$. *Right: Spatial distribution of the absolute error* $|u_{st} - U_{st}^{(\xi)}|$ *over the annulus for the simulation solution compared to the analytical steady solution.*

discretization and is not due to the order of the method chosen to perform the time integration, we have also run the simulations with a first-order explicit (Euler) time-integration method and obtained errors of the same order of magnitude. Figure 4.3 shows the solution to (4.1) obtained at stationary state with the SSB method. Contour lines are also included to illustrate that the no-flux boundary conditions at $r = 1$ and $r = 2$ are satisfied.

The analytical steady state solution of (4.1) also satisfies homogeneous Neumann boundary conditions on the quarter-annulus delimited by $1 \le r \le 2$, $0 \le \theta \le \pi/2$ (see Figure 4.4), which also allows us to use this related geometry to show how the SSB method performs when sharp corners are present in a given geometry. As before, the L^2-norms of the deviations from the analytical steady state are shown in Figure 4.2 (right) for the simulations on the quarter-annulus. Both geometries show similar convergence properties. However, errors are slightly larger than for the full annulus due to the presence of the sharp corners, which become slightly blunted when the smoothed boundary is generated. This is translated into a loss of accuracy of the method from $O(\xi^2)$ to $O(\xi)$ for regions with sharp corners (see interior plot in Figure 4.2, right). This can also be seen in Figure 4.4, which shows the error distribution $|u_{st} - U_{st}^{(\xi)}|$ at steady state over the domain Ω, along with the corresponding solution. See how errors are larger when close to the corners of the domain.

In Figures 4.3 and 4.4, we have shown the solutions of (4.1) within the physical domains of interest, Ω. However, solutions $U^{(\xi)}$ are calculated over the entire extended domain Ω'. Figure 4.5 shows the solutions over Ω' in the full and quarter-annulus examples. While no-flux boundary conditions are implemented along $\partial\Omega$, the overall solution has periodic boundary conditions. Note that, as the solution $U^{(\xi)}$ is not discontinuous on $\partial\Omega$, solutions do not present Gibbs phenomena due to the irregular boundaries.

An important advantage of the SSB method is that when the new formulation given by (3.1) is used, separate equations are not written for the boundaries, as the solution automatically adapts to satisfy the boundary conditions on $\partial\Omega$, which results in a very simple computational implementation. Alterations to the domain geometry therefore can be handled straightforwardly, without generating and implementing additional boundary condition equations. As an example, we present in Figure 4.6
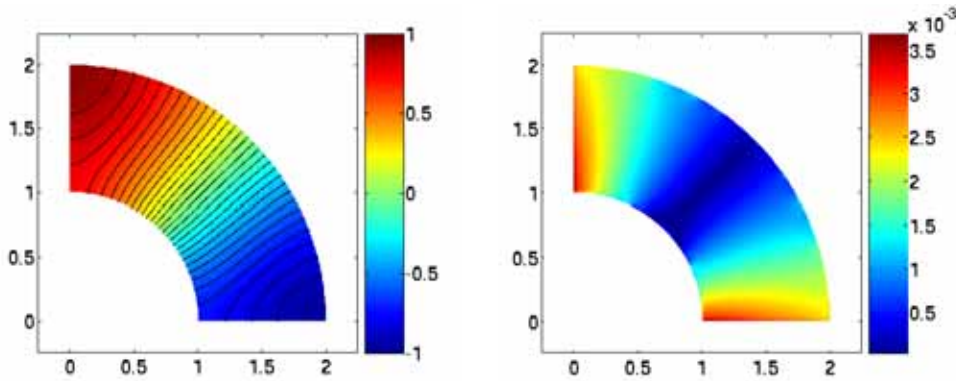
Fig. 4.4. *Left: Solution to (4.1) in the quarter-annulus $1 \le r \le 2$, $0 \le \theta \le \pi/2$ at steady state using the SSB method. Grid resolution is 500×500 and $\xi = 0.025$. Right: Spatial distribution of absolute error $|u_{st} - U_{st}^{(\xi)}|$ over the quarter-annulus for the simulation solution compared to the analytical steady solution.*
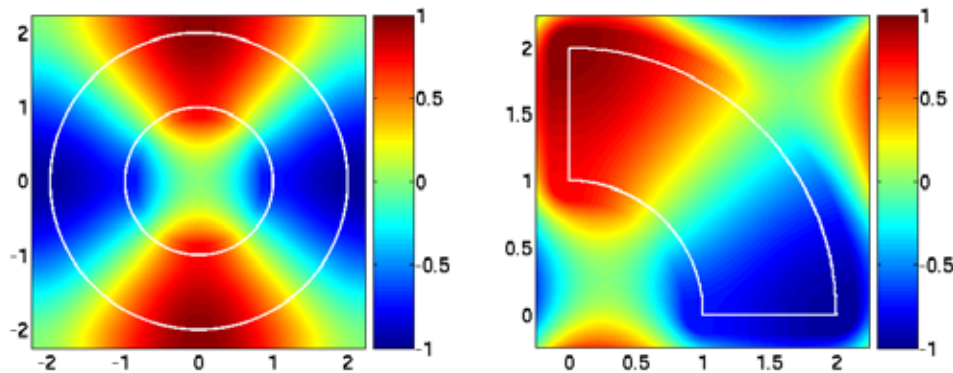

Fig. 4.5. *Solution to (4.1) using the SSB method over the entire domain of integration Ω' for the annulus shown in Figure 4.3 (left) and the quarter-annulus shown in Figure 4.4 (right). Note that the periodicity along $\partial\Omega'$ imposed by the FFT does not alter the solution in Ω or at the boundary $\partial\Omega$ (shown in white), where the zero-flux boundary conditions are satisfied.*

the solution to (4.1) in a more complicated geometry that combines both polar and Cartesian coordinates. As an analytic steady solution to the equation cannot be easily obtained in this domain, we evolve it until time $t = 5$ and compare our solution to the one obtained using finite elements in the finest mesh that our machine could handle (P1-Lagrangian elements, mesh made of 31152 nodes and 61440 triangles). At this resolution, and as shown in Figure 4.6, maximum differences between the solutions obtained by both methods are small.

4.2. The Allen–Cahn equation. An important partial differential equation which arises in the modeling of the formation and motion of phase boundaries is the Allen–Cahn [21] equation

$$
\begin{array}{ll}
(4.3) & \partial_t u = \epsilon^2 \Delta u - f(u), \qquad x \text{ in } \Omega, \\
& \vec{n} \cdot \nabla u = 0, \qquad\qquad x \text{ on } \partial\Omega,
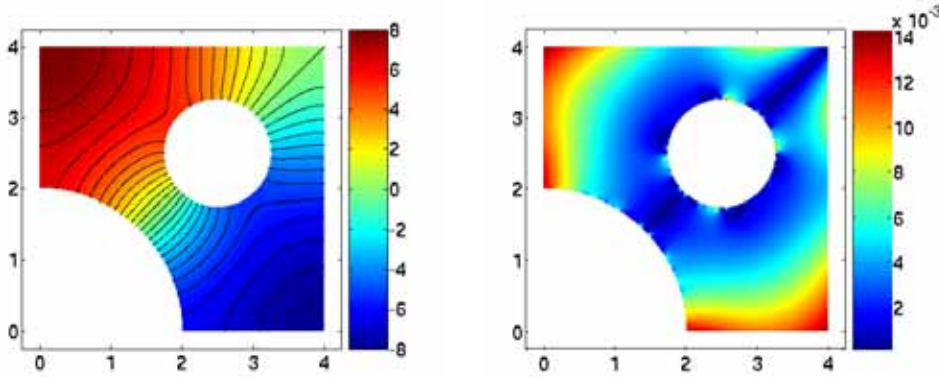\end{array}
$$

FIG. 4.6. *Solution to (4.1) at time $t = 5$ in a more complicated domain (left) and spatial distribution of the difference between the solutions obtained by the SSB method and using finite elements (right). Grid resolution is 400×400 and $\xi = 0.05$.*

where ϵ is a small positive constant and $f(u)$ is the derivative of a potential function $W(u)$ that has two wells of equal depth. For simplicity, we will assume that $W(u) = (u^2-1)^2/4$, which makes $f(u) = u^3-u$. In this manner, the Allen–Cahn equation may be seen as a simple example of a nonlinear reaction-diffusion equation. As explained in [2], this equation has three fixed-point solutions, $u = -1$, $u = 0$, and $u = 1$. The middle state is unstable, but the states $u = \pm 1$ are attracting, and solutions tend to exhibit flat areas close to these values separated by interfaces of increasing sharpness as the control parameter ϵ is reduced to zero. Figure 4.7 shows the solution of the Allen–Cahn equation at $t = 25$ solved with Neumann boundary conditions on an annulus with a z-shaped hole using the SSB method, with $\epsilon = 0.1$. The annulus structure is given by $1 \le r \le 5$ and the z-hole is formed using radii at 2, 3, and 4 and angles in steps of 15 degrees (15, 30, 60, and 75 degrees). As an initial condition, two positive and two negative Gaussian functions located in different parts of the domain were chosen:

$$(4.4) \qquad u(r,\theta,0) = \sum_{i=1}^{n=4} (-1)^{n+1} \exp(-20((x - r_i \cos \theta_i)^2 + (y - r_i \sin \theta_i)^2)),$$

where pairs $(r_1, \theta_1) = (1.5, \pi/6)$, $(r_2, \theta_2) = (4, \pi/12)$, $(r_3, \theta_3) = (4.5, \pi/3)$, and $(r_4, \theta_4) = (4, 11\pi/24)$ represent the positions of the Gaussians in polar coordinates.

For comparison we also solved the Allen–Cahn equation using finite elements in space as in the previous example (P2-Lagrangian elements, mesh made of 8304 elements and 348 boundary elements, 16956 degrees of freedom) and implicit backward differentiation formula for time integration. Due to the sharp transition of the solution between -1 and 1, a slight difference in the position of the interfaces can be seen as a significant error when comparing the solutions obtained by the two methods, but as shown in Figure 4.7 (right) both the SSB and finite elements solutions are in good agreement.

4.3. Reaction-diffusion equations and excitable media. Models of excitable media form another significant class of nonlinear parabolic partial differential equations and describe systems as diverse as chemical reactions [22, 23], aggregation of amoebae in the cellular slime mold *Dictyostelium discoideum* [24], calcium waves
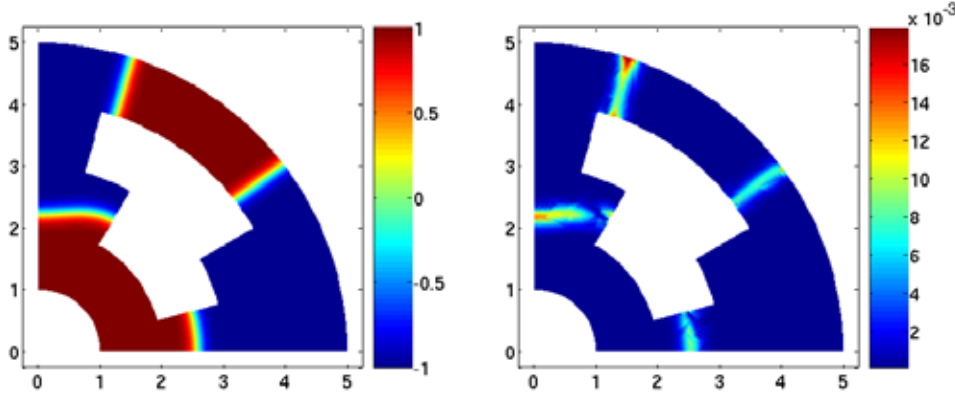
FIG. 4.7. *Solution of the Allen–Cahn equation* (4.3) *at time* $t = 25$ *using the SSB method (left) and errors when compared to the solution obtained using* P2-*Lagrangian finite elements (right). Grid size is* 360×360 *with* $\xi = 0.025$ *for the SSB method.*

[25], and the electrical properties of neural [26] and cardiac cells [27, 28], among others. The equations of excitable systems extend the Allen–Cahn equation by including one or more additional variables that govern growth and decay of the waves. Solutions of excitable media consist of excursions in state space from a stable rest state and a return to rest, with the equations describing the additional variables determining the time courses of excitation and recovery. In spatially extended systems, diffusive coupling allows excitation to propagate as nonlinear waves, and in multiple dimensions complex patterns can be formed, including two-dimensional spiral waves [22, 23, 24, 25, 29] and their three-dimensional analogues, scroll waves [30, 31]. Well-known examples of excitable media equations include the Hodgkin–Huxley [26] model of cells and its generalized simplification, the FitzHugh–Nagumo [32] model.

The dynamics of wave propagation in excitable media has been studied extensively in regular domains. However, the complex geometry inherent to some systems, such as the heart, often can have a significant influence on wave stability and dynamics [33]. This fact, combined with the need for high-order accuracy to resolve the sharp wave fronts characteristic of cardiac models, should make the SSB method a useful tool for studying electrical waves in realistic heart geometries. Figure 4.8 shows an example of a propagating wave of action potential in both an idealized (left) and a realistic (right) slice [34] of ventricular tissue using the SSB method and a phenomenological ionic cell model [31, 33] with equations of the form

$$\text{(4.5a)} \qquad \partial_t u(\mathbf{x}, t) = \nabla \cdot (\boldsymbol{D} \nabla u) - J_{fi}(u, v) - J_{so}(u) - J_{si}(u, w),$$

$$\text{(4.5b)} \qquad \partial_t v(\mathbf{x}, t) = \Theta(u_c - u)(1 - v)/\tau_v^-(u) - \Theta(u - u_c)v/\tau_v^+,$$

$$\text{(4.5c)} \qquad \partial_t w(\mathbf{x}, t) = \Theta(u_c - u)(1 - w)/\tau_w^- - \Theta(u - u_c)w/\tau_w^+,$$

$$\text{(4.5d)} \qquad J_{fi}(u, v) = -\frac{v}{\tau_d}\Theta(u - u_c)(1 - u)(u - u_c),$$

$$\text{(4.5e)} \qquad J_{so}(u) = \frac{u}{\tau_0}\Theta(u_c - u) + \frac{1}{\tau_r}\Theta(u - u_c),$$

$$\text{(4.5f)} \qquad J_{si}(u, w) = -\frac{w}{2\tau_{\text{si}}}(1 + \tanh[k(u - u_c^{\text{si}})]),$$

$$\text{(4.5g)} \qquad \tau_v^-(u) = \Theta(u - u_v)\tau_{v1}^- + \Theta(u_v - u)\tau_{v2}^-,$$
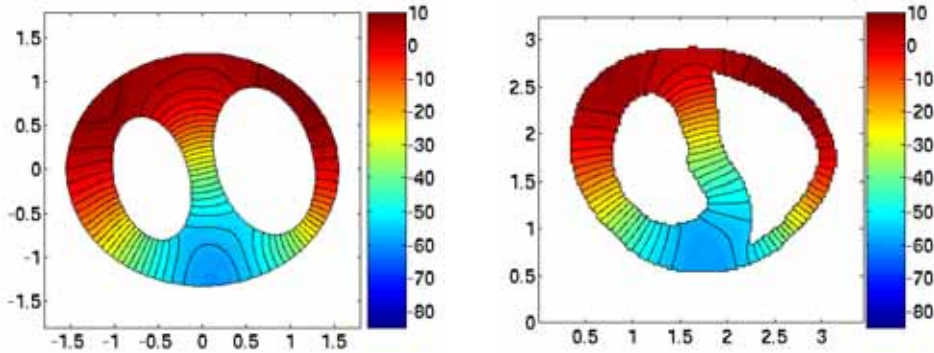
FIG. 4.8. *Propagating wave of electrical potential in an idealized (left) and a realistic (right) slice of ventricular tissue using the SSB method. Grid size is 400×400 and $\xi = 0.025$ in both cases. The color code denotes tissue voltage in mV, where red corresponds to cells with higher potential (depolarization) and blue to cells returning to resting state (repolarization).*
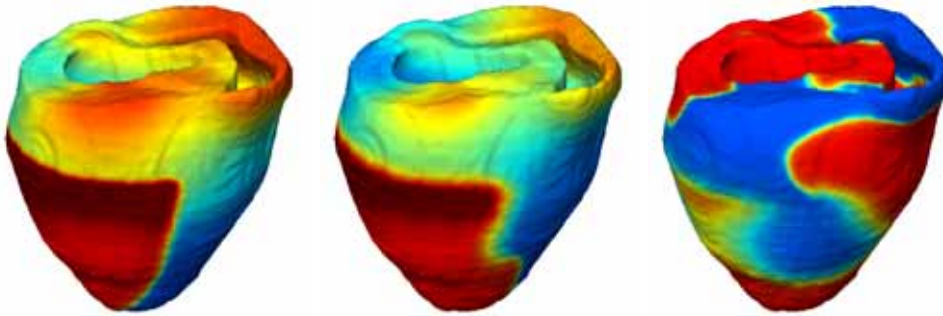

FIG. 4.9. *Propagating wave of electrical potential and generation of a spiral wave in a realistic three-dimensional model of rabbit ventricles using the SSB method. See text for details.*

where u is the membrane potential; J_{fi}, J_{so}, and J_{si} are phenomenological currents; v and w are ionic gate variables; and $\boldsymbol{D}$ is the diffusion tensor (isotropic for these simulations, with value $D = 1$ cm^2/s). In all these formulas, $\Theta(x)$ is the standard Heaviside step function defined by $\Theta(x) = 1$ for $x \geq 0$ and $\Theta(x) = 0$ for $x < 0$, and the set of parameters of the model is chosen to reproduce different cellular dynamics measured experimentally (for simulations presented here, $\tau_d = 0.25$, $\tau_r = 50$, $\tau_{si} = 45$, $\tau_0 = 8.3$, $\tau_v^+ = 3.33$, $\tau_{v1}^- = 1000$, $\tau_{v2}^- = 19.2$, $\tau_w^+ = 667$, $\tau_w^- = 11$, $u_c = 0.13$, $u_v = 0.055$, and $u_c^{si} = 0.85$). Contour lines demonstrate that boundary conditions are correctly approximated by the method in both geometries.

Finally, Figure 4.9 illustrates the application of the proposed method to realistic three-dimensional geometries, using for that purpose the full anatomical model of rabbit heart ventricles. All the information in the ventricular model originally digitalized in a finite elements mesh, including fiber orientation, was interpolated and mapped onto a regular Cartesian grid slightly larger than the structure, of sizes $L_x = 3.4$, $L_y = 3.2$, and $L_z = 3.7$ cm and $150 \times 150 \times 160$ grid points, and smoothed with a value of $\xi = 0.05$. The simulation shows the creation of a spiral wave of electrical activity in the rabbit ventricles, solutions to the reaction-diffusion equations that are

closely related to the development of arrhythmias [29, 31, 33]. In the left image, a second excitation shock is applied in the wake of the preceding excitation wave to initiate the spiral wave. In the first moments the second shock cannot move upwards (central panel) since the tissue has not yet recovered excitability, but starts curving at the bottom of the heart. The right image of Figure 4.9 shows the evolution of the self-maintained spiral wave in the tissue. The simulation is perfectly handled by the SSB method, and the extension of the algorithm is absolutely straightforward from two to three dimensions.

5. Discussion and future work. In this paper, we have presented a new method for implementing homogeneous Neumann boundary conditions using spectral methods for several problems of general interest. The SSB method offers several advantages over finite-difference and finite-element alternatives. Because ghost cells are not needed, the implementation of boundary conditions requires less coding than finite-difference stencils. The use of simple Cartesian grids also makes the SSB method easier to use than finite elements with multiple domain shapes, since *grid generation is not necessary*. Furthermore, the use of FFT routines in the SSB method ensures efficiency and also makes extension of the method to three dimensions straightforward using well-established routines. Since the method is directly based on the FFT, it is very simple to implement on high performance computers by using native parallel or vector FFT libraries.

The most significant limitation of the SSB method is that its accuracy is directly controlled by the value of parameter ξ, and therefore it will be more moderate than the accuracy achieved by any spectral method in a typical rectangular domain. The error of the method also depends directly on the ratio of the width of the smoothed boundary ξ to the spatial step Δx; this implies that when using uniform grids the number of points in the discretization needs to be large. This limitation is perhaps not important for certain classes of problems in which the solution contains steep wavefronts or other sharp features that require a fine spatial resolution to correctly reproduce the dynamics of the system, such as electrical waves in cardiac tissue or shock waves in fluid mechanics. However, for problems with smooth behavior, such as the heat equation with slowly varying sources, the adequate reduction of error in domains with irregular boundaries using this method may require an increase in spatial resolution of a factor of 10 or 20 in each direction of the mesh when compared to what is typically needed to obtain the same accuracy using a spectral method in a rectangular domain. This need for a large number of points is also a clear disadvantage in terms of computational efficiency, and since the accuracy of the method is controlled more by the width of the smoothed boundary rather than by the order of the method used to compute the spatial derivatives, an implementation of the method using a lower order scheme in space, such as the one presented in [18] using finite differences, can be significantly more efficient than the implementation presented here using spectral methods.

Thus, an important future extension of this work is to try to improve the performance of the SSB method for problems that do not track features with sharp spatial gradients. For instance, if the boundary is stationary, it could be useful to compute the spatial derivatives using any numerical scheme featuring adaptability, such as a combination of a nonuniform grid with extra resolution along the boundaries and a nonuniform fast Fourier transform (NFFT), or the use of wavelets [35]. However, if the boundary moves over time, it might be more efficient to use a fine spatial discretization than to keep track of the boundary for such problems. Other planned

future work includes properly handling complex anisotropies in the diffusion matrices, such as those found in cardiac muscle, examining whether the method can be used to satisfy other types of boundary conditions including Dirichlet and Robin, and implementing nonstationary boundaries.

In conclusion, we have presented a new numerical method which imposes homogeneous Neumann boundary conditions in complex geometries using spectral methods. We have used this method to solve various partial differential equations in domains with irregular boundaries and have found good agreement between our solutions and the ones obtained by standard numerical methods. Along with the overall advantage of allowing domains of different shapes to be considered with spectral methods in a very simple way, this method also offers highly accurate discretizations of spatial derivatives, ease of implementation, straightforward extension to three dimensions, and applicability to a wide variety of equations. Moreover, SSB codes need not change to implement different geometries since all the information on the geometry is contained in the function $\phi^{(\xi)}$, with the additional advantage that this function is easy to generate and, unlike finite-element methods, does not require the use of special software for grid generation.

REFERENCES

[1] B. FORNBERG, *A Practical Guide to Pseudospectral Methods*, Cambridge University Press, Cambridge, UK, 1996.

[2] LL. N. TREFETHEN, *Spectral Methods in MATLAB*, SIAM, Philadelphia, 2000.

[3] J. M. SANZ-SERNA, *Fourier techniques in numerical methods for evolutionary problems*, in Proceedings of the 3rd Annual Granada Seminar on Computational Physics, P. L. Garrido and J. Marro, eds., Lecture Notes in Phys. 448, Springer-Verlag, Berlin, 1995, pp. 145–200.

[4] C. CANUTO, M. Y. HUSSAINI, A. QUARTERONI, AND T. A. ZANG, *Spectral Methods in Fluid Dynamics*, Springer-Verlag, Berlin, 1988.

[5] D. GOTTLIEB AND S. A. ORSZAG, *Numerical Analysis of Spectral Methods: Theory and Applications*, SIAM, Philadelphia, 1977.

[6] R. PEYRET, *Spectral Methods for Incompressible Viscous Flow*, Springer-Verlag, New York, 2002.

[7] I. D. ILIEV, E. KH KHRISTOV, AND K. P. KIRCHEV, *Spectral Methods in Soliton Equations*, CRC Press, Boca Raton, FL, 1994.

[8] G. BEN-YU, *Spectral Methods and Their Applications*, World Scientific, River Edge, NJ, 1998.

[9] S. A. ORSZAG, *Spectral methods for problems in complex geometries*, J. Comput. Phys., 37 (1980), pp. 70–92.

[10] K. Z. KORCZAK AND A. T. PATERA, *An isoparametric spectral element method for solution of the Navier-Stokes equations in complex geometry*, J. Comput. Phys., 62 (1986), pp. 361–382.

[11] A. KARMA AND W.-J. RAPPEL, *Quantitative phase-field modeling of dendritic growth in two and three dimensions*, Phys. Rev. E, 57 (1998), pp. 4323–4349.

[12] R. FOLCH, J. CASADEMUNT, A. HERNÁNDEZ-MACHADO, AND L. RAMÍREZ-PISCINA, *Phase-field model for Hele-Shaw flows with arbitrary viscosity contrast.* I. *Theoretical approach*, Phys. Rev. E, 60 (1999), pp. 1724–1733.

[13] R. FOLCH, J. CASADEMUNT, AND A. HERNÁNDEZ-MACHADO, *Phase-field model for Hele-Shaw flows with arbitrary viscosity contrast.* II. *Numerical study*, Phys. Rev. E, 60 (1999), pp. 1734–1740.

[14] A. KARMA, D. KESSLER, AND H. LEVINE, *Phase-field model of mode* III *dynamic fracture*, Phys. Rev. Lett., 87 (2001), 045501.

[15] T. Biben and C. Misbah, *Tumbling of vesicles under shear flow within an advected-field approach*, Phys. Rev. E, 67 (2003), 031908.

[16] R. Gonzalez-Cinca, R. Folch, R. Benitez, L. Ramirez-Piscina, J. Casademunt, and A. Hernandez-Machado, *Phase-field models in interfacial pattern formation out of equilibrium*, in Advances in Condensed Matter and Statistical Mechanics, E. Korucheva and R. Cuerno, eds., Nova Science Publishers, Hauppauge, NY, 2004, pp. 203–236.

[17] M. Frigo and S. G. Johnson, *FFTW: An adaptive software architecture for the FFT*, in Proceedings of the IEEE International Conference on Acoustics, Speech, and Signal Processing, IEEE, Seattle, WA, 1998, pp. 1381–1384.

[18] F. H. Fenton, E. M. Cherry, A. Karma, and W. J. Rappel, *Modeling wave propagation in realistic heart geometries using the phase-field method*, Chaos, 15 (2005), 013502.

[19] A. Bueno-Orovio and V. M. Pérez-García, *Spectral smoothed boundary methods: The role of external boundary conditions*, Numer. Methods Partial Differential Equations, 22 (2006), pp. 435–448.

[20] G. Strang, *On the construction and comparison of difference schemes*, SIAM J. Numer. Anal., 5 (1968), pp. 506–517.

[21] S. M. Allen and J. W. Cahn, *A microscopic theory for antiphase boundary motion and its application to antiphase domain coarsening*, Acta Metall. Mater., 27 (1979), pp. 1085–1095.

[22] A. N. Zaikin and A. M. Zhabotinsky, *Concentration wave propagation in two-dimensional liquid-phase self-oscillating system*, Nature, 225 (1970), pp. 535–537.

[23] M. Bar, Ch. Zlicke, M. Eiswirth and G. Ertl, *Theoretical modeling of spatiotemporal self-organization in a surface catalyzed reaction exhibiting bistable kinetics*, J. Chem. Phys., 96 (1992), pp. 8595–8604.

[24] P. Foerster, S. C. Muller, and B. Hess, *Curvature and spiral geometry in aggregation patterns of Dictyostelium discoideum*, Development, 109 (1990), pp. 11–16.

[25] M. E. Harris-White, S. A. Zanotti, S. A. Frautschy, and A. C. Charles, *Spiral intracellular calcium waves in hippocampal slice cultures*, J. Neurobiol., 79 (1998), pp. 1045–1052.

[26] A. L. Hodgkin and A. F. Huxley, *A quantitative description of membrane current and its application to conduction and excitation in nerve*, J. Physiol., 117 (1952), pp. 500–544.

[27] G. W. Beeler and H. Reuter, *Reconstruction of the action potential of ventricular myocardial fibres*, J. Physiol., 268 (1977), pp. 177–210.

[28] C. Luo and Y. Rudy, *A model of the ventricular cardiac action potential. Depolarization, repolarization, and their interaction*, Circ. Res., 68 (1991), pp. 1501–1526.

[29] J. M. Davidenko, A. M. Pertsov, R. Salomonsz, W. Baxter, and J. Jalife, *Stationary and drifting spiral waves of excitation in isolated cardiac muscle*, Nature, 355 (1992), pp. 349–351.

[30] R. A. Gray, A. M. Pertsov, and J. Jalife, *Spatial and temporal organization during cardiac fibrillation*, Nature, 392 (1998), pp. 75–77.

[31] F. Fenton and A. Karma, *Fiber-rotation-induced vortex turbulence in thick myocardium*, Phys. Rev. Lett., 81 (1998), pp. 481–484.

[32] R. FitzHugh, *Impulses and physiological states in theoretical models of nerve membranes*, Biophys. J., 1 (1961), pp. 445–466.

[33] F. H. Fenton, E. M. Cherry, H. M. Hastings, and S. J. Evans, *Multiple mechanisms of spiral wave breakup in a model of cardiac electrical activity*, Chaos, 12 (2002), pp. 852–892.

[34] F. J. Vetter and A. D. McCulloch, *Three-dimensional analysis of regional cardiac function: A model of rabbit ventricular anatomy*, Prog. Biophys. Mol. Biol., 69 (1998), pp. 157–183.

[35] S. Bertoluzza, *An adaptive collocation method based on interpolating wavelets*, in Multiscale Wavelet Methods for Partial Differential Equations, W. Dahmen, A. J. Kurdila, and P. Oswald, eds., Academic Press, New York, 1997, pp. 109–135.